Available online at www.sciencedirect.com
SCIENCE DIRECT®
Journal of Nuclear Materials 319 (2003) 65–73
journal of nuclear materials
www.elsevier.com/locate/jnucmat

# Thermal annealing behaviour and defect evolution of helium in fully stabilised zirconia

P.M.G. Damen [a,*], A. van Veen [b], F. Labohm [b], H. Schut [b], M.A. van Huis [b]

[a] European Commission, Joint Research Centre, Institute for Transuranium Elements, P.O. Box 2340, D-76125 Karlsruhe, Germany
[b] Interfaculty Reactor Institute, Delft University of Technology, Mekelweg 15, 2629 JB Delft, The Netherlands

**Abstract**

Helium implantations in fully stabilised zirconia have been performed with 30 keV ions with high doses ($5.1 \times 10^{16}$ and $2.6 \times 10^{16}$ cm$^{-2}$) and low doses ($6.3 \times 10^{15}$ and $1.7 \times 10^{15}$ cm$^{-2}$). The retained amount of helium and depth profiles have been monitored with neutron depth profiling and the damage distribution with positron beam analysis (PBA) after several annealing steps. The temperature dependent helium release was investigated by thermal helium desorption spectrometry. In the low dose samples, helium is released through diffusion as seen by a broadening of the helium distribution peak. PBA, performed with a two-layer model, shows shrinkage of the damage layer during annealing. For the high dose samples the helium peak does not broaden after annealing. Helium is retained up to high temperatures which is ascribed to bubble formation during thermal annealing. Fitting of the PBA results to a three-layer model shows that the ion implanted layer gets narrower after annealing at 600 K, up to 1000 K the *S*-parameter is increasing because helium is released from the bubbles, whereby vacancy clusters are left behind.


## 1. Introduction

Presently, zirconia, fully stabilised with yttria (FSZ, $ZrO_2$–$Y_2O_3$), is a favoured material for the use as an inert matrix material for actinide transmutation and as a host material for nuclear waste storage. As an actinide host, the material is attractive because cubic $UO_2$ and $PuO_2$ are isostructural with cubic $ZrO_2$ and actinides are soluble in zirconia. Secondly, rare-earth sesquioxides (like $Er_2O_3$ and $Gd_2O_3$) are soluble in zirconia as well [1]. This gives the possibility to dope an actinide-bearing zirconia waste- or fuel-form with rare-earth atoms, which can serve as depletable neutron absorbers [2].

As a fuel matrix, the zirconia is subject to neutron exposure, gamma and beta radiation, fission fragment damage and self-irradiation by alpha-decay from the incorporated actinides. The effects of neutron exposure were already studied in 1955 [3] and also recently work has been performed on neutron irradiated zirconia [4]. Fission fragment damage has been studied in detail employing ion irradiations. FSZ has been implanted with xenon [5–9], iodine [2,9–12] and cesium [11–14].

The effects of helium on the stability of such ceramics have not been studied in much detail [15,16]. Damen et al. [15] have presented thermal desorption experiments for helium implanted FSZ combined with neutron depth profiling (NDP) measurements. In this paper, the behaviour of helium in FSZ under thermal treatment is discussed in more detail and possible release mechanisms are described.

## 2. Experimental procedure

### 2.1. Sample preparation and damage distribution

Sintered samples of FSZ with atomic composition $Zr_{0.90}Y_{0.10}O_{1.95}$ and a density of 5.8 g cm$^{-3}$ were polished

* Corresponding author. Tel.: +49-7247 951 486; fax: +49-7247 951 99650.
*E-mail address:* damen@itu.fzk.de (P.M.G. Damen).

0022-3115/03/$ - see front matter 
doi:10.1016/S0022-3115(03)00135-1

Table 1
Overview of investigated samples and applied analyses

| Sample | Gas | He-dose ($cm^{-2}$) | Investigation method[a] | Range (nm) | Peak displacements (dpa) | Average He-density ($cm^{-3}$) | Maximum He-density ($cm^{-3}$) |
|---|---|---|---|---|---|---|---|
| I | $^3$He | $1.7 \times 10^{15}$ | NDP/PBA | 168 | 0.05 (at 126 nm) | $5.4 \times 10^{19}$ | $1.2 \times 10^{20}$ |
| II | $^3$He | $6.3 \times 10^{15}$ | NDP/PBA | 168 | 0.18 (at 126 nm) | $2.0 \times 10^{20}$ | $4.3 \times 10^{20}$ |
| III | $^3$He | $2.6 \times 10^{16}$ | NDP/PBA | 168 | 0.73 (at 126 nm) | $8.3 \times 10^{20}$ | $1.8 \times 10^{21}$ |
| IV | $^3$He | $5.1 \times 10^{16}$ | NDP/PBA | 168 | 1.46 (at 126 nm) | $1.6 \times 10^{21}$ | $3.4 \times 10^{21}$ |
| V | $^4$He | $1.7 \times 10^{15}$ | THDS | 180 | 0.05 (at 132 nm) | $5.4 \times 10^{19}$ | $1.0 \times 10^{20}$ |
| VI | $^4$He | $6.3 \times 10^{15}$ | THDS | 180 | 0.18 (at 132 nm) | $1.9 \times 10^{20}$ | $3.7 \times 10^{20}$ |
| VII | $^4$He | $2.6 \times 10^{16}$ | THDS | 180 | 0.73 (at 132 nm) | $8.2 \times 10^{20}$ | $1.5 \times 10^{21}$ |
| VIII | $^4$He | $5.1 \times 10^{16}$ | THDS | 180 | 1.46 (at 132 nm) | $1.6 \times 10^{21}$ | $3.0 \times 10^{21}$ |

The helium range and the peak displacements as calculated by SRIM-2000.
[a] PBA: positron beam analysis; NDP: neutron depth profiling; THDS: thermal helium desorption spectrometry.

down to a surface roughness less than 1 μm and subsequently annealed at 1673 K for 2 h. These samples were implanted at room temperature at the Interfaculty Reactor Institute (IRI) with either $^3$He or $^4$He with a He-flux of $3 \times 10^{12}$ $cm^{-2}\,s^{-1}$. The helium ion fluences varied between $1.7 \times 10^{15}$ and $5.1 \times 10^{16}$ $cm^{-2}$, the implantation energy used was 30 keV. An overview of the samples is given in Table 1.

To estimate the defect and helium distribution after implantation, calculations have been performed using the SRIM-2000 code [17], where for FSZ, a displacement energy of 40 eV was used [18]. Results of these calculations are shown in Table 1 as well. The average He-density has been calculated over width of the helium peak. The region between the surface and the helium implanted region has not been taken into account in this calculation.

### 2.2. Thermal helium desorption spectrometry

The samples implanted with $^4$He (samples V–VIII) have been subjected to thermal helium desorption spectrometry (THDS) in the HDS1, one of the desorption facilities of IRI. The principle of this set up is based on the measurement of the helium partial pressure increase in a small oven. The sample is put in a very small crucible made of tungsten and this crucible is heated up through electron bombardment. The temperature of the crucible is monitored with a thermocouple. A delay in the temperature of the sample with respect to the crucible was observed. However, the data presented in this article have been corrected for this temperature delay. The helium released from the sample is detected with a quadrupole mass spectrometer. Samples have been ramp-annealed at a heating rate of 1 $K\,s^{-1}$ to pre-defined maximum temperatures. Before annealing to the next (higher) temperature the sample was allowed to cool down to room temperature.

### 2.3. Neutron depth profiling and positron beam analysis

The samples implanted with $^3$He (samples I–IV) have been investigated with the NDP technique [19,20], to find the depth-dependent helium profile, and with positron beam analysis (PBA) [21] after various annealing stages. The thermal annealing was performed in air, using a heating rate of 15 $K\,min^{-1}$. After reaching the pre-defined temperature it was kept constant for half an hour after which the oven was switched off and cooled down by unforced cooling.

In the case of $^3$He the NDP technique is based on the reaction:

$$^3\mathrm{He} + n \rightarrow {}^3\mathrm{H} + \text{proton (572 keV)} \quad (1)$$

where the proton is detected by a Si-detector facing the helium irradiated surface. The measured kinetic energy of the protons depends on the distance it has to travel from the position where it is created to the sample surface. Since the initial energy of the proton (and the Triton particle) is known, the measured energy loss yields the depth of the $^3$He particle. The energy distribution of the protons can be fitted very well with a Gaussian and, as the detector response is also a Gaussian (FWHM 12 keV), it is reasonable to assume that the $^3$He distribution is Gaussian as well. In that case the true energy spectrum is described by a Gaussian with a FWHM given by quadratically subtracting the FWHM of the detector from the FWHM of the spectrum. (see Fig. 1(A)). From the energy spectrum, by making use of the stopping powers, the depth distribution can be calculated, as shown in Fig. 1(B), again showing the corrected and uncorrected peaks.

With PBA, the generation and evolution of defects can be monitored. A mono-energetic positron beam was used and the energy of the positrons was varied between 0.1 and 25 keV. If the implantation energy of the positron is increased, the average depth at which a positron

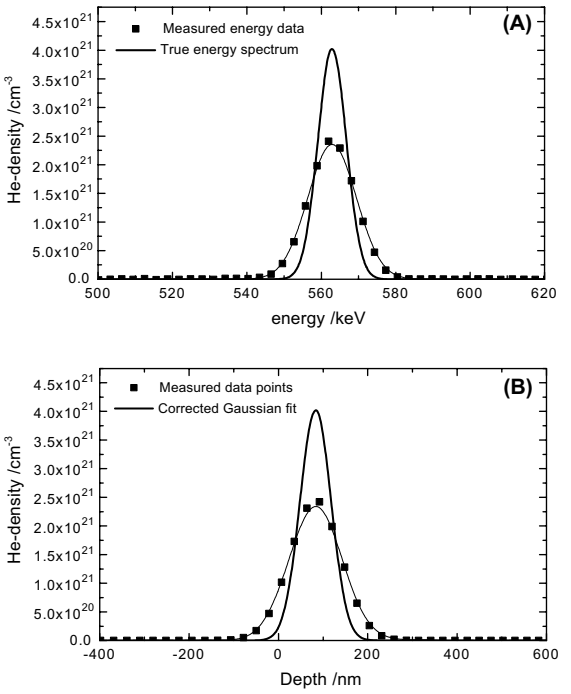


Fig. 1. The correction of the FWHM of the NDP results. (A): The measured energy profile (markers) and the fit of these data (thin line) are corrected for the detector resolution (thick line); (B): the transformation of the uncorrected and corrected energy spectra into a depth profile. The markers indicate the measured data points and the thin line through the markers is a Gaussian fit of these data.

is thermalised and ultimately annihilates via the emission of two 511 keV photons, increases. In this way, depth-dependent defect information can be obtained [21]. Positrons have a high affinity to be trapped at sites with reduced atomic density such as vacancies. The presence of such a defect changes the local electron momentum distribution. In a PBA Doppler Broadening measurement this is seen as a broadening (or narrowing) of the 511 keV photo peak with respect to the undisturbed solid. The shape of this broadening profile is quantified by the so-called $S$- and $W$-parameters. The $S$-parameter gives the fractional area under the centre of the peak and it represents the fraction of annihilations with low momentum electrons, such as valence and conduction electrons. The $W$-parameter gives the ratio between the area under the wings and the total area and is thus sensitive to the fraction of high momentum electrons, in general core electrons.

A positron that annihilates in a local open volume (such as a vacancy type defect or vacancy agglomerate (void)) has a lower probability to interact with core electrons. The $S$-parameter then increases with respect to the $S$-parameter of a defect-free sample. For the value of the $W$-parameter the opposite is observed [20]. In this analysis only the $S$-parameter is used.

## 3. Results

### 3.1. Neutron depth profiling

From the NDP measurements the total amount of helium (Fig. 2(A)), the width of the helium distribution (Fig. 2(B), corrected for the detector resolution, as discussed in Section 2.3) and the mean depth (Fig. 2(C)) were obtained, where the error in the maximum annealing temperature is less than 20 K.

For sample I (lowest He-dose $1.7 \times 10^{15}$ cm$^{-2}$) the FWHM of the distribution increases with increasing

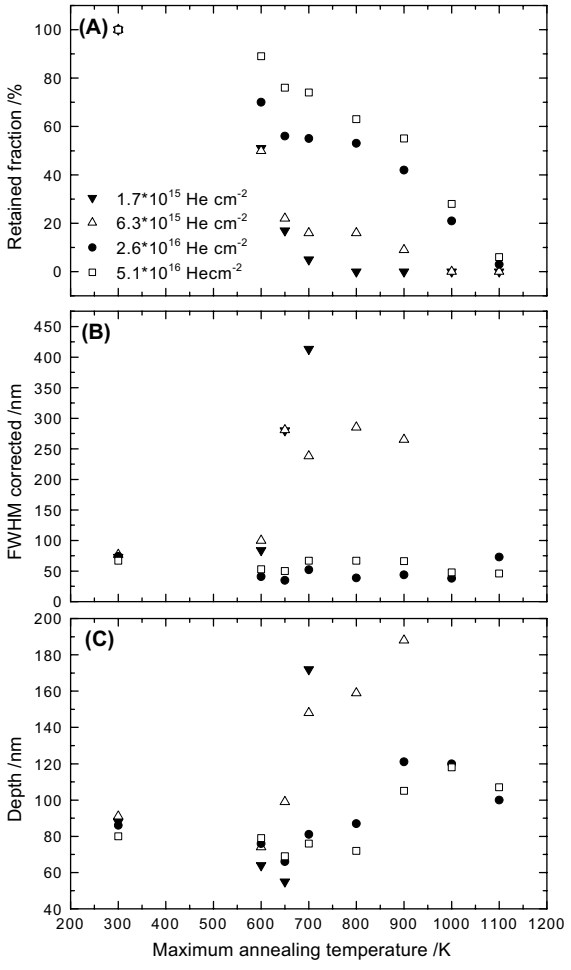


Fig. 2. Results obtained from the NDP-measurements. (A): The retained fraction vs. the maximum annealing temperature; (B): the corrected FWHM of the helium peak and (C): the depth of the maximum of the Gaussian fit of the helium peak.

annealing temperature. After annealing at 700 K, the centre of the peak has shifted considerably towards the inside of the sample, but it should be mentioned, that the distribution was not Gaussian anymore.

For sample II ($6.3 \times 10^{15}$ cm$^{-2}$) after thermal annealing a broadening of the helium distribution peak is observed as an increase in the FWHM, typical for a diffusional process. The centre of the peak shifts towards the inner side of the sample with increasing annealing temperatures. After annealing at 700 K, only 16% of the helium initially present in the material is retained. This does not change after the next annealing step. After annealing at 1000 K all the helium has been annealed out.

For samples III (He-dose $2.6 \times 10^{16}$ cm$^{-2}$) and IV (He-dose $5.1 \times 10^{16}$ cm$^{-2}$), helium is retained up to much higher temperatures than in sample I and II. In addition the FWHM of the peak does not increase with increasing annealing temperature and only a slight shift of the maximum of the peak towards the inner side of the sample is observed. These samples had to be annealed up to 1200 K before all the helium had been annealed out.

### 3.2. Thermal helium desorption spectrometry

The samples for THDS were annealed stepwise, the heating rate used was about 1 K s$^{-1}$ and the maximum temperature was increased for every step.

In Fig. 3, for samples II (He-dose $6.3 \times 10^{15}$ cm$^{-2}$) and IV (He-dose $5.1 \times 10^{16}$ cm$^{-2}$), the retained fraction after every annealing step is plotted as a function of the maximum annealing temperature, both for NDP (squares) as well as for THDS (circles). It can be observed that in the NDP experiments, helium is released at lower temperatures than in the case of THDS. In THDS, the sample is heated with a heating rate of 1 K s$^{-1}$ until the maximum annealing temperature (as plotted on the abscissa) is reached. Then the sample is cooled down immediately; i.e. the sample is only several seconds at its maximum temperature. In the annealing of the samples used for NDP, the sample is kept about half an hour at its maximum temperature, which gives the helium more time to be released from the sample. For sample I (He-dose $1.7 \times 10^{15}$ cm$^{-2}$, no figure) a shift of about 100 K between the NDP and THDS experiments is observed. In the NDP experiments, the sample is empty after annealing at 800 K, in the THDS experiments, this case is reached at a temperature that is about 80 K higher. The results for sample III (He-dose $2.6 \times 10^{16}$ cm$^{-2}$) are comparable to those of sample IV (He-dose $5.1 \times 10^{16}$ cm$^{-2}$).

In Fig. 4(A)–(D), the results of the desorption experiments are shown. Here it can clearly be seen that for the lowest dose sample, all helium is released in one peak at low temperature, as confirmed by NDP experiments.

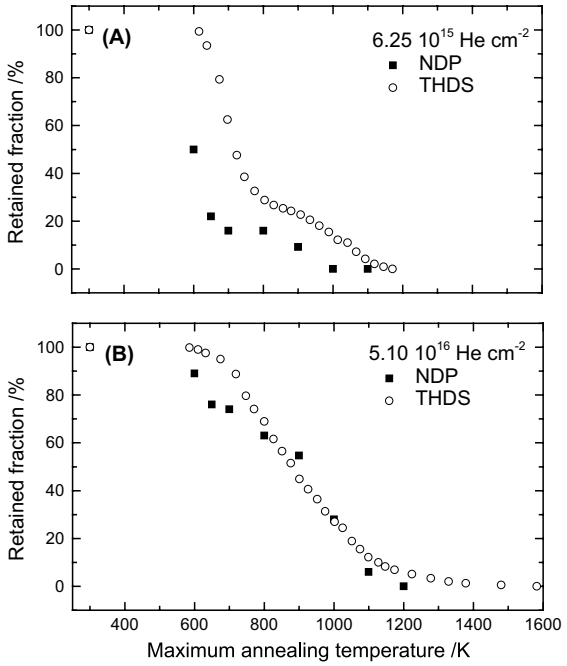


Fig. 3. Results of NDP (squares) and THDS (circles). Plotted is the retained fraction of helium vs. the maximum annealing temperature. (A): The results for samples II (NDP) and VI (THDS) and (B): the results for samples IV (NDP) and VIII (THDS).

In Fig. 3(A), a change in slope for sample VI was observed, which indicates helium release in two stages. In Fig. 4(B), these two stages can clearly be seen. The first release peak is finished at about 850 K, then the second release peak is visible until about 1150 K. For the samples VII and VIII (Fig. 4(C) and (D), respectively), quite a sudden start of the helium release is observed. But a large portion of the helium is retained up to very high temperatures. A similar observation has been made for 200 keV and 1 MeV implanted helium in FSZ in Ref. [15].

When the release is a first order desorption process, the time dependent release can be described as:

$$\frac{dN}{dt} = -N \cdot f \tag{2}$$

with $N(t)$ the number of helium atoms retained in the sample at time $t$, $f = f_0 \exp(-Q/kT)$ the temperature dependent release frequency with $f_0$ the pre-factor, $k$ the Boltzmann constant, $T$ the temperature and $Q$ the activation enthalpy for diffusion. The change in $N$ will be very small if only the first part of the release curve is considered. Then it can be assumed that $N$ is constant and equal to $N_{0,i}$, which is the amount of helium at the begin of the annealing step $i$. Plotting the logarithm of the release rate vs. $1/T$ shows Arrhenius behaviour.

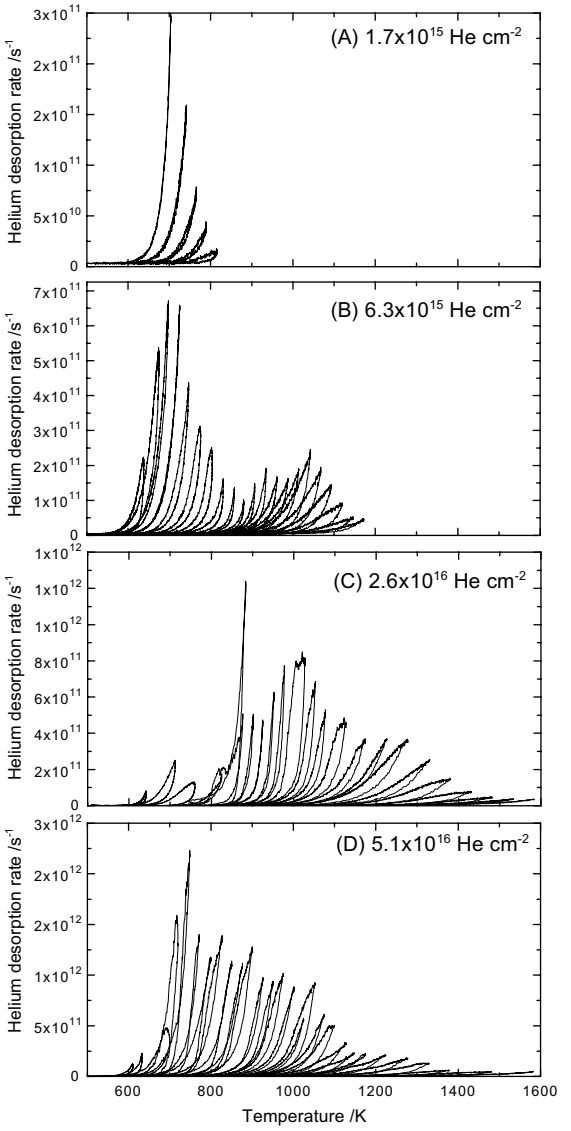


Fig. 4. Partial desorption spectra from the THDS measurements for samples V (top figure) to VIII (lower figure). The helium desorption rate is plotted vs. the annealing temperature; both the heating and cooling are shown.

From the slopes of the curves the activation enthalpy $Q$ can derived; the pre-exponential factor $f_{0,i}$ can be derived from the amount of helium at the beginning of the annealing step ($N_{0,i}$) and the intersection with the line $1/T = 0$ [22].

In Fig. 5(A) and (B), the Arrhenius behaviour of sample VI (Fig. 5(A), with He-dose $6.3 \times 10^{15}$ cm$^{-2}$) and sample VIII (Fig. 5(B), with He-dose $5.1 \times 10^{16}$ cm$^{-2}$) is shown. On the abscissa the value of $1000/T$ is given, and for clarity, the abscissa at the top gives the temperature. In Fig. 6 the activation enthalpy $Q$ and pre-factors $f_{0,i}$

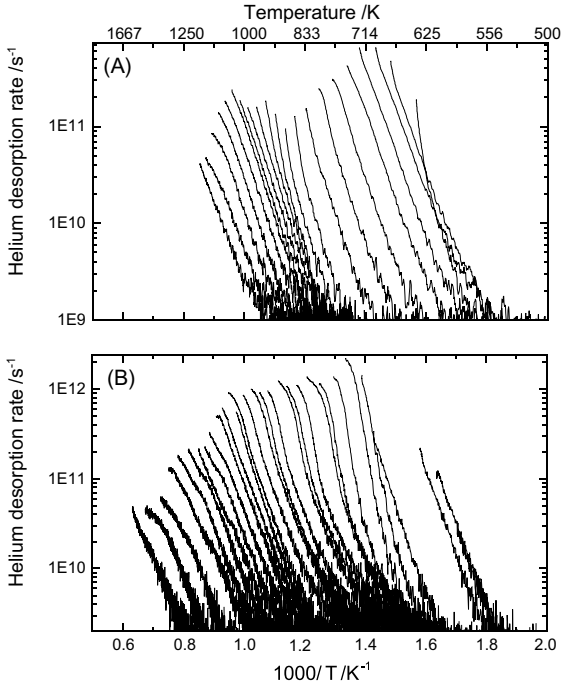


Fig. 5. Arrhenius plot for (A): sample VI (He-dose $6.3 \times 10^{15}$ cm$^{-2}$) and (B): sample VIII (He-dose $5.1 \times 10^{16}$ cm$^{-2}$). The helium desorption rate is plotted vs. $1000 \cdot T^{-1}$. For clarity, the temperature is given at the abscissa at the top.

are given for the samples V–VIII, as obtained from the Arrhenius figures. The top part of the figure (A) shows the retained fraction as function of the maximum annealing temperature, where it can be clearly seen that for the lowest dose sample (sample V, with He-dose $1.7 \times 10^{15}$ cm$^{-2}$) all the helium is released at low temperatures. In Fig. 6(B), the activation enthalpies that were calculated from the slopes from the Arrhenius plots are given for all four doses.

From the figures the following remarks can be made:

- For the lowest He-fluence (sample V, $1.7 \times 10^{15}$ cm$^{-2}$, solid triangles) the activation enthalpy is almost the same for all annealing steps. It has an average value of 1.93 eV. The logarithm of the pre-exponential varies between 9.4 and 11.7, with an average of 10.8. In general, this value is decreasing with increasing temperature.
- For sample VI (He-dose $6.3 \times 10^{15}$ cm$^{-2}$, open triangles) all helium is released at 1200 K as seen in Fig. 6(A). The activation enthalpy varies between 1.69 and 2.27 eV, with an average of 2.0 eV where the low temperature data are in general smaller than the average, and the high temperature data are larger. The logarithm of the pre-exponential factor for low temperatures is of the same order of magnitude as

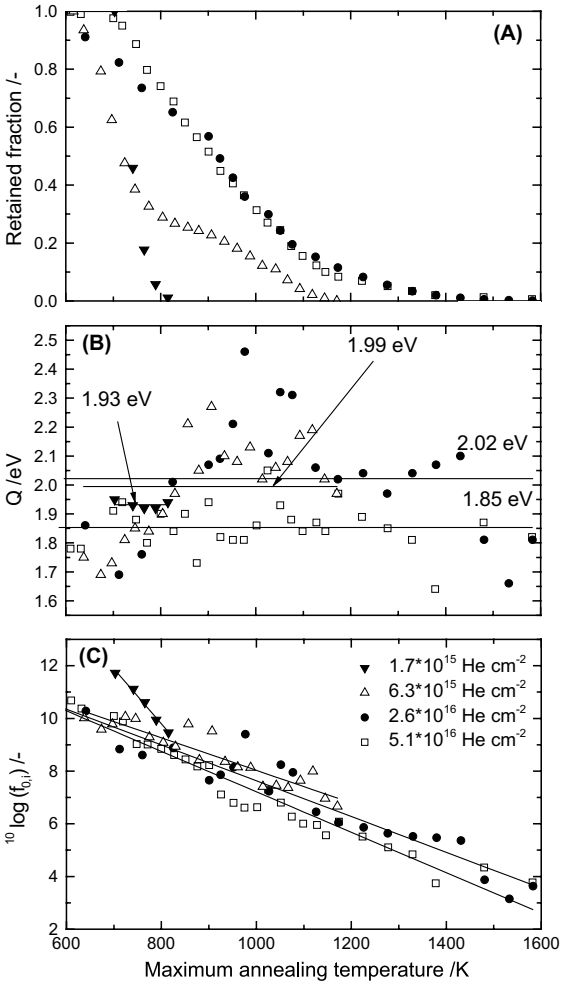


Fig. 6. Calculated pre-factors $f_{0,i}$ and activation enthalpies $Q$ for samples V–VIII vs. the maximum annealing temperature of the desorption step. (A): The retained fraction of helium; (B): the activation enthalpies for all annealing steps are given and (C): the pre-factors $f_{0,i}$, in the form of $^{10}\log f_{0,i}$, are given.

the value for sample V (He-dose $1.7 \times 10^{15}$ cm$^{-2}$). With increasing temperature, the logarithm of the pre-exponential factor decreases more or less linearly with increasing temperature.

- For sample VII (He-dose $2.6 \times 10^{16}$ cm$^{-2}$, closed circles) and sample VIII (He-dose $5.1 \times 10^{16}$ cm$^{-2}$, open squares) the release rates vs. temperature have more or less the same profile for both samples. The calculated activation enthalpies are for both samples scattered around their average, 2.02 eV for sample VII and 1.85 eV for sample VIII. The logarithm of the pre-exponential factor of both samples shows the same behaviour as for sample VI. It decreases with increasing annealing temperature.

It was shown that the activation enthalpy for all four samples is more or less the same, while there is a difference in the pre-exponential factor depending on the implanted helium dose and the annealing temperature. In general, for higher annealing temperatures, the frequency pre-factor gets smaller. A similar behaviour of the pre-exponential factor has been observed for helium implanted silicon in Ref. [23] and will be discussed in Section 4.

### 3.3. Positron beam analysis

The PBA technique was applied to samples I–IV (i.e. the same samples as used for the NDP investigations). The NDP investigations were stopped when all the helium from the sample was released, but the PBA investigations were continued to see whether the open volumes introduced by the implantation would disappear.

In Fig. 7(A) and (B), a selection of the measured $S$-profiles for samples II (Fig. 7(A), with He-dose $6.3 \times 10^{15}$ cm$^{-2}$) and IV (Fig. 7(B), with He-dose $5.1 \times 10^{16}$ cm$^{-2}$) are shown. The markers indicate the measured data points, the solid lines are the fitting results as obtained with the programme VEPFIT [24,25]. The $S$-parameter profile of sample I (He-dose $1.7 \times 10^{15}$

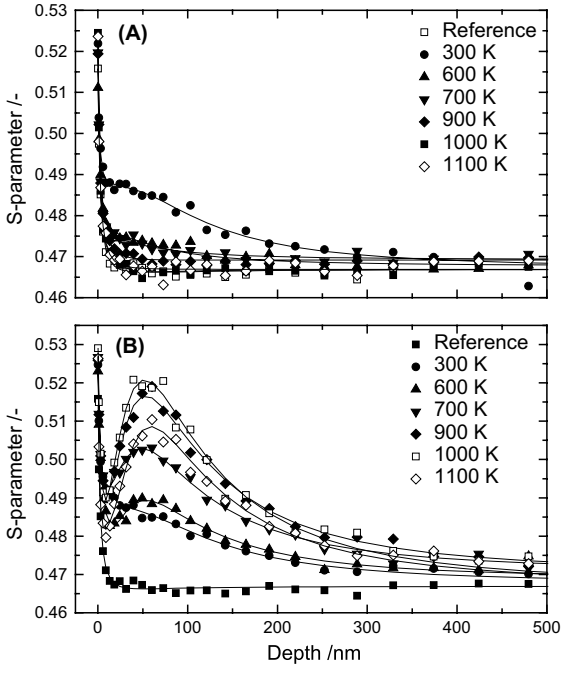


Fig. 7. Measured $S$-profiles for (A): sample II (He-dose $6.3 \times 10^{15}$ cm$^{-2}$) and (B): sample IV (He-dose $5.1 \times 10^{16}$ cm$^{-2}$) after various annealing temperatures. The markers given in the figure are the measured data, the lines through the markers are the fitting results as obtained with the programme VEPFIT.

$cm^{-2}$) develops more or less similar to the *S*-profile for sample II (He-dose $6.3 \times 10^{15}$ $cm^{-2}$) and the same can be said about samples III (He-dose $2.6 \times 10^{16}$ $cm^{-2}$) and IV (He-dose $5.1 \times 10^{16}$ $cm^{-2}$). With the PBA technique, the difference between the two samples implanted with the lower dose samples (I and II) and the higher dose samples (III and IV) can clearly be seen. For the low dose sample (top figure) after implantation (circles) the *S*-parameter is larger than for the unimplanted reference material. After thermal annealing, however, the *S*-parameter decreases gradually towards the *S*-parameter of the unimplanted sample. For the *S*-parameter of the high dose sample, instead of observing a decrease in the *S*-parameter, the *S*-parameter increases further, with its maximum at a depth of about 60 nm.

The results as obtained with the PBA technique have been analysed with the programme VEPFIT [24,25] and these results are shown in Fig. 8 for all four implanted doses. The two lowest dose samples have been fitted with a two-layer model, the two high dose samples with a three-layer model, where the last layer is the bulk material, which has a fixed *S*-value.

In the top part of Fig. 8 the *S*-parameter for each layer is shown, where the dashed line shows the *S*-parameter of the bulk material. The lower Fig. 8(B) gives the thickness of each layer, where layer 1 is the surface layer. From Fig. 8(B), it can be seen that after implantation (300 K) the damage layer has a thickness between 110 and 155 nm. From Fig. 8 the following is observed:

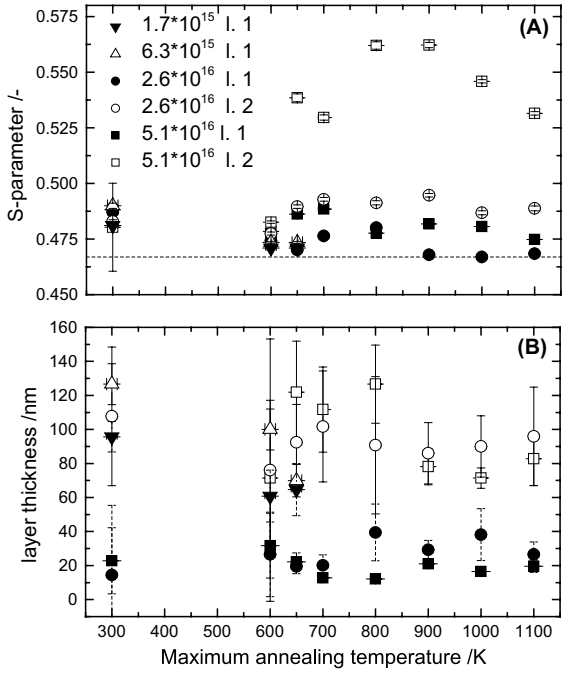


Fig. 8. Results as obtained with the programme VEPFIT for samples I–IV after various annealing temperatures. (A): The *S*-parameter for each layer is given as function of the maximum annealing temperature. The dashed curve gives the *S*-value for the bulk material and (B): the thickness for each zone in the material.

- For the low dose samples, the *S*-parameter of the layer has a value slightly larger than the *S*-parameter of the bulk material and with increasing annealing temperature; the *S*-parameter decreases towards the bulk value. Already after annealing at 700 K the difference in *S*-value between the damage layer and the bulk cannot be distinguished by VEPFIT. For both low dose samples the thickness of the damage layer gets narrower after thermal annealing.
- For the high dose samples, not much change in the *S*-parameter and thickness of layer 1 is observed. However, it can clearly be seen that the second layer becomes narrower after each annealing step (which has also been observed by NDP), and that its *S*-parameter increases. The release of bubbles leaves large open volumes behind. We have to anneal up to 1000 K before the *S*-parameter starts decreasing again.

## 4. Discussion

Due to the addition of $Y^{3+}$ into $ZrO_2$, oxygen vacancies are created in the matrix. The region between the surface and the helium implantation zone will contain point defects like $V_O$, $V_{Zr}$ and $V_Y$ as well as Frenkel pairs, F-centres and complementary hole centres. During the helium implantations, a preferential forward momentum transfer occurs to interstitials, which might cause an interstitial excess concentration in the implantation direction and of vacancy excess in the opposite direction. The activation enthalpy for self-diffusion of $O^{2-}$ in FSZ has been determined by Fox et al. to be about 1 eV [26] which is much lower than the 2 eV as measured for helium.

The peak displacements vary between 0.05 dpa (lowest dose) and 1.46 dpa (highest dose) as shown in Table 1. After implantation, it is expected that helium is trapped in vacancies and vacancy clusters. By means of TEM, helium bubbles have not been observed for FSZ as-implanted with a He-dose of about $10^{16}$ $cm^{-2}$ [27].

- In the case of the lowest dose samples (samples I and V, He-dose $1.7 \times 10^{15}$ $cm^{-2}$), the peak displacement damage is about 0.05 dpa. The helium will be trapped mostly in oxygen vacancies. The increase in *S*-parameter after implantation can be explained by an increase in open volumes mostly in the form of single vacancies. The maximum helium density for this dose is 0.13 at.%. During thermal annealing, helium is released by dissociation from the vacancy and subsequently by vacancy assisted diffusion towards the

surface. Note that a large concentration of oxygen-vacancies exists in this material. By means of NDP a broadening of the helium peak was shown, typical for diffusion. After annealing at 700 K, the *S*-parameter has almost reached the *S*-value of the reference sample. Apparently, the vacancies introduced by this low dose implantation are very mobile and can be easily removed by thermal annealing.

- For samples II and VI ($6.3 \times 10^{15}$ He cm$^{-2}$) the *S*-profile after implantation does not differ much from the lowest dose samples. Helium is trapped in vacancies and vacancy clusters. By NDP, a broadening of the helium distribution was observed; typical for a diffusional process. Then, by NDP and THDS we see that a small fraction of the helium is retained up to higher temperatures, but by NDP we see that the centre of the broadened peak has shifted to a larger depth. A small fraction of the initially implanted helium is trapped in bubbles.
- For samples III and IV (He-dose $2.6 \times 10^{16}$ cm$^{-2}$) (and VII and VIII, He-dose $5.1 \times 10^{16}$ cm$^{-2}$), there is hardly any variation in the *S*-profile immediately after implantation compared to the *S*-profiles of samples I and II. In THDS it was shown that the helium is retained up to high temperatures. This has also been shown by NDP; the helium distribution does not broaden and at high temperatures the maximum of the distribution shifts towards a larger depth. Instead of diffusing towards the surface, the helium gets trapped in bubbles. We propose that at the temperatures where for the lowest dose case the helium diffusion starts, Ostwald ripening occurs. During thermal annealing, small clusters dissociate and larger ones grow at the expense of the smaller ones. This process will continue until nanosize bubbles are present. TEM pictures of bubbles in FSZ implanted with 35 keV He-ions with a dose of $10^{17}$ He cm$^{-2}$ after annealing are shown in Ref. [16]. At higher temperatures, starting between 700 and 800 K, helium starts to be released from the bubbles, as seen by NDP. However, as seen with NDP, helium is released slowly from the bubbles, and the *S*-parameter of the damage layer increases with every annealing step. This can be explained by the open volumes left behind by the bubbles, yielding a high *S*-value. Cavities have developed up to a depth of about 120 nm, which is lower than the helium implantation depth as predicted by TRIM. This is explained by the fact that the helium has to move towards shallower depth in order to combine with vacancies.

## 5. Summary and conclusions

Fully stabilised zirconia was implanted with either $^3$He or $^4$He at four different doses. For the samples implanted at low He-dose ($\approx 10^{15}$ cm$^{-2}$), helium is released at low temperatures with an activation enthalpy of about 2 eV. A broadening of the helium distribution was observed with NDP. The small defects introduced by the implantation can be easily removed by thermal annealing as observed with PBA. From the two-layer model, used to model the PBA results, it can be seen that after every annealing step, the first layer gets thinner and its *S*-parameter decreases toward the *S*-parameter of the bulk material. For the samples implanted with He-doses in the order of $10^{16}$ cm$^{-2}$, it can be seen that part of the helium is retained up to high temperatures. From NDP investigations no broadening of the helium distribution was seen, instead the FWHM of the distribution peak stays almost constant. For the analysis of the PBA results a three-layer model was used. After thermal annealing the second layer shrinks slightly and its *S*-parameter increases due to a clustering of defects in the helium rich zone. For all four investigated doses, a decrease in the pre-exponential jump factor $f_{0,i}$, with increasing temperature was observed. This can be explained as follows. The pre-exponential factor is the product of an attempt frequency ($\nu$) which is of the order of the Debye-frequency ($10^{12}$–$10^{13}$ s$^{-1}$), and the entropy factor $\exp(\Delta S/k)$. Since $\Delta S$ is the difference between the entropy of the final state and the initial state of the helium it can turn strongly negative when helium jumps from a bubble (very high entropy) to a very localised position in a vacancy (low entropy) [28].

The activation enthalpy was measured to be about 2 eV. Depending on the implanted dose, helium is released between about 600 and 1200 K. In a reactor, irradiation temperatures of 1000 K are not uncommon. Thus, the helium formed in the zirconia-matrix due to α-decay of actinides will migrate in the fuel during irradiation with neutrons in a nuclear reactor. The helium will either migrate to the gap between cladding and fuel or be trapped in bubbles, most likely together with the fission gases krypton and xenon. The migration of helium towards the gap between the cladding and the fuel does not have to be a problem, as long as the fuel pins are designed in such a way to be able to accommodate the helium produced.

In the experiments described in this article, the maximum helium density in the sample was about 4 at.%. (helium atoms per matrix atom). If we compare this to the EFTTRA-T4 [29] experiments, after irradiation, the helium density was 0.5 at.% (helium atom per matrix atom). In the case of the high dose samples, annealing up to high temperatures is necessary to remove the damage caused by the implantation of the helium. During reactor irradiation, apart from the damage caused by α-decay, more importantly, the damage caused by neutrons, fission products, recoil atoms and β-decay should be accounted for. Although from the implantation experiments it is observed that FSZ

behaves well with respect to damage caused by fission products and α-decay, real irradiation experiments have to be performed to study the stability of FSZ in a more realistic situation.

## Acknowledgements

The authors would like to thank Technische Keramik Thayngen METOXIT AG, for providing the material investigated in this article.

## References

[1] A. Rouanet, Rev. Int. Hautes. Temper. Et. Refract. 8 (1971) 161.
[2] K.E. Sickafus, Hj. Matzke, K. Yusadu, P. Chodak III, R.A. Verrall, P.G. Lucuta, H.R. Andrews, A. Turos, R. Fromknecht, N.P. Baker, Nucl. Instrum. and Meth. B 141 (1998) 358.
[3] G.E. Klein, 1. X-ray examination of ceramic samples. 2. Operation of the shielded X-ray diffractometer, Oak Ridge National Laboratory, Oak Ridge, TN, Solid State Division Semiannual Progress Report, ORNL-1852, 1955.
[4] B. Savoini, D. Cáceres, I. Vergara, R. González, J.E. Muñoz Santiuste, J. Nucl. Mater. 277 (2000) 199.
[5] C. Degueldre, M. Pouchon, M. Döbeli, K. Sickafus, K. Hojou, G. Ledergerber, S. Abolhassani-Dabras, J. Nucl. Mater. 289 (2001) 115.
[6] K.E. Sickafus, C.J. Wetteland, N.P. Baker, N. Yu, R. Devanathan, M. Nastasi, N. Bordes, Mater. Sci. Eng. A 253 (1998) 78.
[7] K. Yasuda, M. Nastasi, K.E. Sickafus, C.J. Maggiore, N. Yu, Nucl. Instrum. and Meth. B 136 (1998) 499.
[8] N. Yu, K.E. Sickafus, P. Kodali, M. Nastasi, J. Nucl. Mater. 244 (1997) 266.
[9] K.E. Sickafus, Hj. Matzke, Th. Hartmann, K. Yusuda, J.A. Valdez, P. Chodak III, M. Nastasi, R.A. Verrall, J. Nucl. Mater. 274 (1999) 66.
[10] M. Pouchon, M. Döbeli, C. Degueldre, Nucl. Instrum. and Meth. B 148 (1999) 783.
[11] L.M. Wang, S.X. Wang, S. Zhu, R.C. Ewing, J. Nucl. Mater. 289 (2001) 122.
[12] C. Degueldre, M. Pouchon, M. Doebli, G. Ledergerber, Mater. Res. Soc. Symp. Proc., vol. 540, p. 337.
[13] M. Pouchon, M. Döbeli, C. Degueldre, M. Burghartz, J. Nucl. Mater. 274 (1999) 61.
[14] M. Pouchon, C. Degueldre, M. Döbeli, Prog. Nucl. Energy 38 (2001) 275.
[15] P.M.G. Damen, Hj. Matzke, C. Ronchi, J.P. Hiernaut, T. Wiss, R. Fromknecht, A. van Veen, F. Labohm, Nucl. Instrum. and Meth. B 191 (2002) 571.
[16] N. Sasajima, T. Matsui, S. Furuno, T. Shiratori, K. Hojou, Nucl. Instrum. and Meth. B 166&167 (2000) 250.
[17] J.F. Ziegler, J.P. Biersack, U.L. Littmark, The Stopping Power and Range of Ions in Solids, Pergamon, New York, 1985, The calculations presented in this paper used the SRIM-2000 version.
[18] L.M. Wang, S.X. Wang, S. Zhu, R.C. Ewing, J. Nucl. Mater. 289 (2001) 122.
[19] H. Schut, A. van Veen, F. Labohm, A.V. Federov, E.A.C. Neeft, R.J.M. Konings, Nucl. Instrum. and Meth. B 147 (1999) 212.
[20] E.A.C. Neeft, A. van Veen, R.P.C. Schram, F. Labohm, Prog. Nucl. Energy 38 (2001) 287.
[21] A. van Veen, H. Schut, P.E. Mijnarends, in: P. Coleman (Ed.), Positron Beams and their Applications, World Scientific, Singapore, 2000, p. 191 (Chapter 6).
[22] P.M.G. Damen, A. van Veen, Hj. Matzke, H. Schut, J.A. Valdez, K.E. Sickafus, C.J. Wetteland, J. Nucl. Mater. 306 (2002) 180.
[23] S. Godey, E. Ntsoenzok, T. Sauvage, A. van Veen, F. Labohm, M.F. Beaufort, J.F. Barbot, Mater. Sci. Eng. B 73 (2000) 54.
[24] A. van Veen, H. Schut, J. de Vries, R.A. Hakvoort, M.R. IJpma, in: P.J. Schultz, G.R. Massoumi, P.J. Simpson (Eds.), AIP 218, Positron Beams for Solids and Surfaces, 1990, p. 171.
[25] H. Schut, A. van Veen, Appl. Surf. Sci. 85 (1995) 225.
[26] A.C. Fox, T.W. Clyne, Surf. Coat. Techn., accepted for publication.
[27] P.M.G. Damen, T. Wiss, A. van Veen, R. Fromknecht, in preparation.
[28] A. van Veen, in: S.E. Donelly, J.H. Evans (Eds.), Fundamental Aspects of Inert Gases in Solids, Plenum, New York, 1991, p. 41.
[29] T.A.G. Wiss, P.M.G. Damen, J.P. Hiernaut, submitted to J. Nucl. Mater.